Micro-Spec: an ultracompact, high-sensitivity spectrometer for far-infrared and submillimeter astronomy

Giuseppe Cataldo,* Wen-Ting Hsieh, Wei-Chung Huang, S. Harvey Moseley, Thomas R. Stevenson, and Edward J. Wollack

NASA Goddard Space Flight Center, 8800 Greenbelt Road, Greenbelt, Maryland 20771, USA

*Corresponding author: Giuseppe.Cataldo@nasa.gov

High-performance, integrated spectrometers operating in the far-infrared and submillimeter ranges promise to be powerful tools for the exploration of the epochs of reionization and initial galaxy formation. These devices, using high-efficiency superconducting transmission lines, can achieve the performance of a meter-scale grating spectrometer in an instrument implemented on a 4 inch silicon wafer. Such a device, when combined with a cryogenic telescope in space, provides an enabling capability for studies of the early universe. Here, the optical design process for Micro-Spec (μ-Spec) is presented, with particular attention given to its two-dimensional diffractive region, where the light of different wavelengths is focused on the different detectors. The method is based on the stigmatization and minimization of the light path function in this bounded region, which results in an optimized geometrical configuration. A point design with an efficiency of ~90% has been developed for initial demonstration and can serve as the basis for future instruments. Design variations on this implementation are also discussed, which can lead to lower efficiencies due to diffractive losses in the multimode region.   © 2014 Optical Society of America

OCIS codes: (050.1940) Diffraction; (120.6200) Spectrometers and spectroscopic instrumentation; (220.2740) Geometric optical design; (300.6340) Spectroscopy, infrared.

http://dx.doi.org/10.1364/AO.53.001094

1. Introduction

Far-infrared (IR) and submillimeter (15 μm–1 mm) spectroscopy provides a powerful tool to probe a wide range of environments in the universe. In the past 30 years, many space-based observatories, such as Spitzer, Herschel, and the Infrared Space Observatory (ISO) [1–3], have opened the far-IR window to the universe, revealing rich line and continuum spectra from objects ranging from interplanetary dust particles to major galactic mergers and young galaxies in the early universe. Discoveries made by these observatories have provided unique insights into physical processes leading to the evolution of the universe and its contents. However, many questions remain unanswered regarding the very first moments of the universe, as well as galactic, stellar, and planetary formation.

Micro-Spec (μ-Spec) is proposed as a technology concept to enable new discoveries in the far-IR spectral range. μ-Spec will be a high-sensitivity, direct-detection spectrometer operating in the 450–1000 μm regime. The light from the telescope is coupled to the spectrometer chip via a broadband slot antenna (Fig. 1) and directed to the power splitters and delay network realized in microstrip transmission lines. These microstrip elements are connected to a planar waveguide multimode region via transitions, which also serve as internal feed apertures. The planar waveguide multimode region has two internal antenna arrays, one for transmitting and one for receiving the spectrum as a function of wavelength. Absorber structures lining the
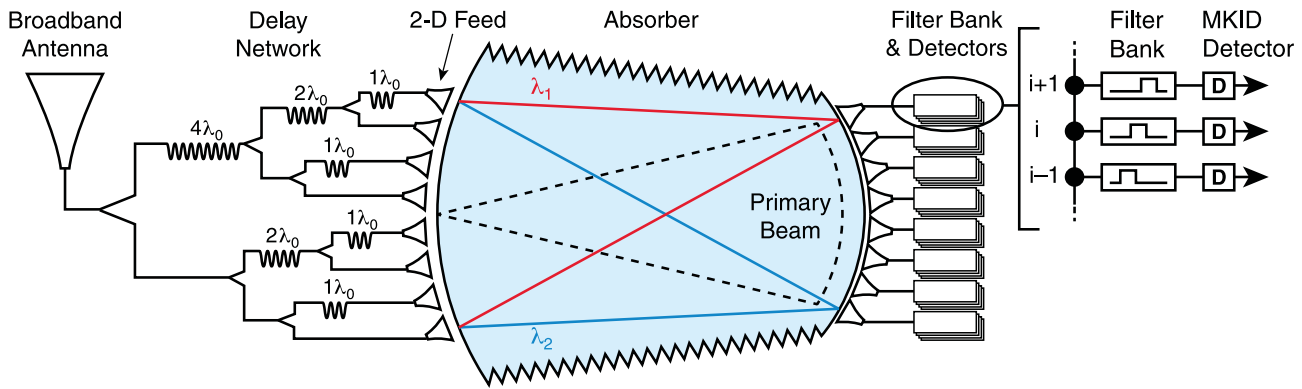
Fig. 1. Layout of the µ-Spec module. The power is coupled into the instrument using a broadband antenna (left). It is then transmitted through a low-loss superconducting transmission line to a divider and a phase delay network, which creates a retardation across the input to the multimode region (in light blue). The feed horns will radiate a converging circular wave, which will concentrate the power along the focal surface, with different wavelengths at different locations. The outputs are connected to a bank of order-sorting filters to disentangle the various orders.

multimode region are used to control the power emitted into large angles or reflected from the receiver antenna array. Finally, each receive antenna in the multimode region is coupled to a bank of order-sorting filters terminated in microwave kinetic inductance detectors (MKIDs) for readout. The instrument, with a resolution $\mathcal{R} \sim 1200$, will be integrated on a 4 inch diameter (100 mm) silicon chip. This reduction in size is largely realized through the use of single-mode microstrip delay lines, which can be relatively compactly routed on the silicon wafer. Relative to counterparts realized in free space, the required transmission line lengths are more compact by a factor of the medium's effective index. For all these reasons, µ-Spec can become an important instrument capability under the low background conditions realized in balloon and space-borne platforms such as the Space Infrared Telescope for Cosmology and Astrophysics (SPICA) [4]. The spectral range of the implementation studied here is set by the materials employed for the transmission line and detectors. Application of this approach is presently confined to wavelengths $\lambda > 250$ µm by the gap frequency of available low-loss superconductors. These include niobium (Nb) and niobium-titanium nitride (NbTiN) for the transmission line structures and molybdenum nitride (MoN) for the detectors.

Two distinct electromagnetic modes are used in the µ-Spec transmission spectrometer: microstrip and parallel-plate waveguide [5] (see Fig. 4, right). Microstrip is a single-mode transmission line structure that is utilized in its dominant quasi-transverse electromagnetic mode (TEM) and in this context is analogous to single-mode fiber optic. It is used to realize the electrical delay line network. The parallel-plate waveguide has a TEM symmetry, and the region serves as a multimode spatial power combiner. Its function can be compared to a grating spectrometer [6], in which a plane wave is reflected from the grating and the phase of each partial wave scattered from the rulings is a linear function of position across the grating. µ-Spec thus differs from similar technologies by

the order of processing of the light in the spectrometer. For instance, in a Rowland spectrometer the required phase retardation is generated by reflection from the grating grooves [6–10], whereas in Z-Spec, which is an example of planar Rowland grating architecture, propagation occurs in parallel-plate waveguides [11–14]. A last comparison can be made with one-dimensional bootlace lenses found in microwave practice [15–18], which µ-Spec builds upon for sub-millimeter wave applications.

In this work, the detailed optical design of the µ-Spec transmission spectrometer is presented. We begin in Section 2 with an outline of the multimode power-combiner region optical design, then describe the internal two-dimensional feed structures used to couple from microstrip lines to this multimode region in Section 3, and finish by bringing these elements together to compute the modeled response of the entire antenna array in Section 4.

2. Detailed Spectrometer Design

The performance of the spectrometer is optimized by the selection of the x and y coordinates of each radiator and a differential phase shift on each delay line. In the case of the Rowland spectrometer, two points on the focal surface can be chosen and wavelengths assigned to them [11,12]. The x and y positions of the grooves in the grating can be selected to provide zero phase errors at each of these stigmatic points. A similar constructive approach can be used in the case of µ-Spec, where each emitter has an additional degree of freedom, the phase shift at the radiator, which allows generating a third stigmatic point. In the case of the Rowland grating, the selection of wavelengths at the two stigmatic points determines the dispersion of the grating.

In µ-Spec, the selection of the wavelengths of three stigmatic points determines both the dispersion and the linearity of the dispersion of the system. A constraint on the selection is required if linear dispersion is desired. In the case presented here, the stigmatic points and their associated wavelength

were chosen to provide relatively linear dispersion and good imaging over the wavelength range of interest. The positions and wavelengths of the stigmatic points are free parameters and can be selected to optimize aspects of the instrument performance. A reasonable choice, which is adopted here, is to select points that minimize the overall root-mean-square (RMS) phase error for all spectrometer outputs (Fig. 3).

In the prototype version of the instrument described here, in order to fit four spectrometers in a 100 mm silicon wafer, each in a 25 mm × 25 mm region, the maximum radius allowed is $R = 1.25$ cm. This choice is not optimal but enables several designs to be experimentally studied within a single mask set and the development of the required fabrication process. The overall design was therefore carried out with the parameters shown in Table 1, where values for an initial design (A) and its optimized version (B) here adopted as the baseline are shown.

With these parameters, the design procedure described was implemented in MATLAB through the goal attainment method of Gembicki [19]. This method was chosen because its implementation enables the resolution of vectorial equations subject to nonlinear constraints that arise in the case presented in this paper. The following set of equations describes the propagation of light through the spectrometer,

$$F_m(\mathbf{x}) = F_m^*, \qquad m = 1, ..., 3N_e, \tag{1}$$

where F_m represents the electrical delay that must be equal to F_m^*, an integer multiple of the wavelengths, at the three stigmatic points. N_e represents the number of radiators, and $3N_e$ equations are needed to calculate the electrical delay of all radiators at each of the three stigmatic points. The vector of the unknowns, $\mathbf{x}$, consists of the coordinates x_i and y_i of the N_e emitters' centers and the electrical path lengths in silicon, R_i^e, for each feed horn delay line.

Table 1. Spectrometer Parameter Summary[a]

Global Design Parameters:			
Minimum frequency, $f_1 = c/\lambda_{o1}$		450	[GHz]
Maximum frequency, $f_2 = c/\lambda_{o2}$		650	[GHz]
Silicon, relative permittivity, ε_r		11.7	
Maximum wavelength in silicon, $\lambda_1 = \lambda_{o1}/\sqrt{\varepsilon_r \mu_r}$		195	[μm]
Minimum wavelength in silicon, $\lambda_2 = \lambda_{o2}/\sqrt{\varepsilon_r \mu_r}$		135	[μm]
Blaze point wavelength in silicon, $\lambda_B = \sqrt{\lambda_1 \lambda_2}$		164	[μm]
Resolving power, $\mathcal{R}$		65	
Grating Order, M		1	
Design Variation:	A	B	
Number of emitters, N_e	65	65	
Number of receivers, N_r	47	65	
Antenna array element spacing or pitch, p	179	161	[μm]
Multimode region, physical radius, R	1.25	1.05	[cm]

[a]Speed of light in vacuum, $c = 3.0 \times 10^8$ m/s.

Constraints are necessary to limit the search of the solution in the correct parameter space. In fact, each of the system's equations is of order 2 and the search of the solution was restricted within $\lambda_1/40$ from the geometric optics solution for the grating solution (the $2R$ dotted arc on the left side of Fig. 2). Using a numerical as opposed to an analytical solution thus allows us to analyze and incorporate the channel isolation and higher-order diffractive response into the optimization (see Section 3). Indeed, while the feed phase centers reside on the position of the analytical solution, it will be shown that the array response is not uniform in angle.

All quantities in Eq. (1) are defined as follows:

$$F(\mathbf{x}) = \begin{bmatrix} R_i^e + R_{1i}^e - R_1^e \\ R_i^e + R_{2i}^e - R_2^e \\ R_i^e + R_{Bi}^e - R_B^e \end{bmatrix} \qquad i = 1, ..., N_e$$

is the light path function matrix ($3N_e \times 1$), whose first $2N_e$ rows are associated with stigmatic points 1 and 2 respectively, and the last N_e rows with the blaze point B. All quantities in the $F(\mathbf{x})$ matrix represent electrical lengths in the transmission medium. For example, the terms in the first N_e rows associated with stigmatic point 1 are indicated below:

• R_i^e is the electrical path length of the i-th silicon microstrip delay line;
• $R_{1i}^e = [\sqrt{(R\sin\beta_1 - x_i)^2 + (R\cos\beta_1 - y_i)^2}] \times \sqrt{\varepsilon_r \mu_r}$ is the electrical path length of the i-th feed horn from stigmatic point 1 in the silicon parallel-plate waveguide multimode region;
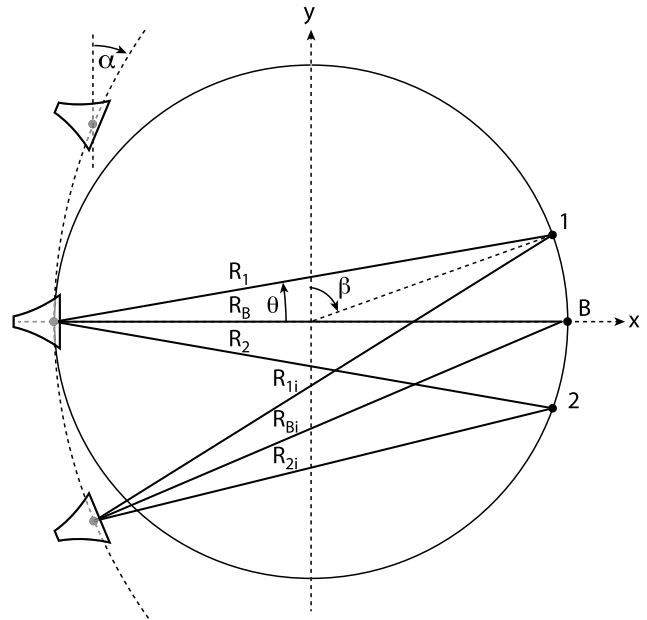

Fig. 2. Simplified representation of the grating geometry. On the left side three radiators can be seen, which point to the blaze point, B. The path from each radiator's phase center to the first and second stigmatic points are also indicated by solid lines for the array's i-th and center reference feed.

- $R_1^e = [R\sqrt{(1 + \sin \beta_1)^2 + \cos^2 \beta_1}] \times \sqrt{\varepsilon_r \mu_r}$ is the reference electrical path length of stigmatic point 1 from the central feed horn ($i = (N_e + 1)/2$), in the silicon multimode region.

A 0.45 µm thick monocrystalline silicon dielectric substrate is employed on the chip. The electrical length in the parallel-plate waveguide region is computed from the product of the index of refraction in the medium and the physical length defined by the geometry in Fig. 2. For example, $R_{1i}^e = R_{1i}\sqrt{\varepsilon_r \mu_r}$, where ε_r and $\mu_r \approx 1$ are the effective relative permittivity and permeability specifying the propagation in the guiding medium. The parallel-plate waveguide conductor and ground plane are well approximated and modeled as perfect electric conductors (PEC). A surface reactance was assigned to the superconductor (niobium) to account for the kinetic inductance and model its influence on the impedance and propagation constant in the microstrip transmission line structures. The superconducting material was modeled as a 0.2 µm thick layer with a London penetration depth $\lambda_L = 95$ nm [20]. Similar definitions apply to stigmatic point 2 and the blaze point B. Finally,

$$F^* = \begin{bmatrix} \left(i - \frac{N_e + 1}{2}\right)M\lambda_{o1} \\ \left(i - \frac{N_e + 1}{2}\right)M\lambda_{o2} \\ \left(i - \frac{N_e + 1}{2}\right)M\lambda_{oB} \end{bmatrix} \quad i = 1, \dots, N_e,$$

where $M = 1$ represents the order of the grating chosen for this design and λ_o the free-space wavelengths of the three stigmatic points. Here, the presence of subscript o signifies the radiation wavelength in free space and without indicates in the dielectric medium as defined in Table 1. In order to maximize the instrument efficiency, the emitters are tilted by an angle α so as to point to the center of the focal surface (Fig. 2):

$$\alpha_i = -\arctan\left(\frac{y_i}{|x_i| + R}\right). \tag{2}$$

A particular solution is found when placing the emitter antennas on the $2R$ circle, using an axisymmetric configuration, and placing the blaze point on the optical axis. This provides a partial diagonalization of the problem, as in [15]. Under these hypotheses, indeed, the last N_e equations of Eq. (1), which refer to the blaze point, can be explicitly rewritten as shown below:

$$R_i^e + \left[\sqrt{(R \sin \beta_B - x_i)^2 + (R \cos \beta_B - y_i)^2} - R_B \right]$$
$$\times \sqrt{\varepsilon_r \mu_r} = \left(i - \frac{N_e + 1}{2}\right)M\lambda_{oB}, \tag{3}$$

where β_B is the angle between the y axis and the line from the center of the Rowland circle to the blaze point (Fig. 2). Here $\beta_B = \pi/2$, which yields

$$R_i^e + \left[\sqrt{(R - x_i)^2 + y_i^2} - R_B \right] \times \sqrt{\varepsilon_r \mu_r}$$
$$= \left(i - \frac{N_e + 1}{2}\right)M\lambda_{oB}. \tag{4}$$

Now, the terms $\sqrt{(R - x_i)^2 + y_i^2}$ express the distance of the i-th feed horn from the blaze point. Because the emitters lie on the $2R$ circle, this quantity is exactly equal to $2R$. Also R_B is equal to $2R$ given the axisymmetric configuration of the instrument and the particular location chosen for the blaze point. Therefore, these two terms cancel out and one readily obtains

$$R_i^e = M\lambda_{oB}\left(i - \frac{N_e + 1}{2}\right), \tag{5}$$

which is a linear relation between the electric length in silicon, R_i^e, and the feed horn number, i.

To find the precise spacings of the emitters along the grating circle needed in order to satisfy the stigmatic equation for the pair of symmetric off-axis stigmatic points at the specified high and low wavelengths, our numerical solution method shows that the spacing between adjacent antennas is not a constant but grows quadratically as a function of position. In design example A, a change of ~13 µm from the nominal design value, $p = 179$ µm, is observed. This is the same behavior found by Rotman and Turner [15], who derived an analytical solution for the analogous design of a bootlace lens and found that the problem reduces to solving an ordinary quadratic equation, from which one can determine the antenna positions.

As mentioned in the beginning of this section, the diffractive solution can be found by restricting the algorithm to searching for radiator positions within a limited distance from the ideal Rowland circle. The constraint reads

$$\left| \sqrt{(x_i - R)^2 + y_i^2} - (2R + z) \right| \leq \lambda_1/40, \tag{6}$$

where z is the phase center correction provided by finite-element simulations ($z = 15$ µm, see Section 4) and $\lambda_1/40 \sim 5$ µm is chosen to provide the upper and lower bounds. This is equivalent to a phase error of $(2\pi/\lambda_{o1}) \times (\lambda_{o1}/40)$ rad $\sim 1/6$ rad.

Having selected the nine parameters, i.e., the coordinates of the stigmatic points and their wavelengths, we proceed to determining the locations and phase shifts of the radiators. The geometry of a Rowland spectrograph was chosen as a starting point, with the radiators on a surface of radius $2R$ and the detectors on a circle of radius R at a distance of $2R$ from the center of the radiators. Finally, the spacing of the radiators is a free parameter and will typically be chosen to limit diffraction losses. We begin with a first radiator near the center of the radiator circle. Next, we choose an adjacent radiator and

perturb its position and differential phase, which results in arriving at each of the three stigmatic points. This procedure is continued for the radiators on each of the delay lines. This results in zero phase error at the stigmatic points by construction, low RMS phase errors between the stigmatic points, and diffraction-limited performance in the multimode region over the design spectral range. The RMS phase error, φ_{RMS}, is illustrated in Fig. 3 for design A, and it was calculated by assuming a uniform weight for each radiator at each point on the focal plane:

$$\varphi_{\mathrm{RMS}}(\theta_j) = \left[\sum_{i=1}^{N_e} \frac{(\varphi_{ij} - \langle \varphi(\theta_j)\rangle)^2}{N_e}\right]^{1/2}. \qquad (7)$$

Here, φ_{ij} is the relative phase of each transmitter, $\langle \varphi(\theta_j)\rangle = 0$ is the relative phase of the central transmitter (this is zero by construction as the central radiator is used as a reference, i.e., $F^*_{(N_e+1)/2} \equiv 0$), N_e is the number of transmitters, and θ_j represents the angle corresponding to each of the points in which the focal plane was discretized. The phase between the i-th transmitter and the j-th point on the receiver focal plane is defined as $\varphi_{ij} = 2\pi\sqrt{\varepsilon_r\mu_r}/\lambda_{oj} \times F_i$ and λ_{oj} is the free-space wavelength.

3. Antenna Feed Response

Conceptually, each microstrip feed structure is a two-dimensional analog of an adiabatic feed horn. To achieve the desired performance, the feed needs to match impedance, modal shape, and angular resolution over the design frequency band. An adiabatic impedance taper [21] for the input microstrip line width to the output is achieved via a Hecken taper [22], which is a near-optimum matching section in the sense that it approaches an "equal-ripple" response without the use of abrupt discontinuities. These properties lower its sensitivity to fabrication variations and tolerances. This feed section serves
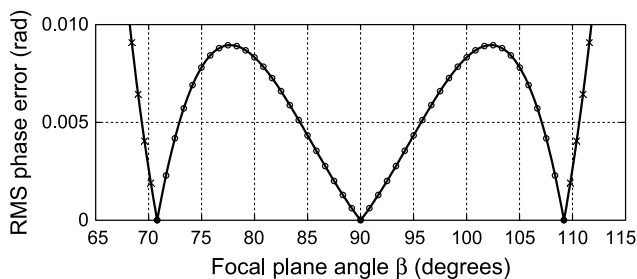

Fig. 3. RMS phase error between the average and the phase of all other transmit feed paths evaluated as a function of receiver position with the design parameters in Table 1 for design A. The RMS phase error vanishes at the three stigmatic points by construction and remains low in between. This ensures diffraction-limited performance over the power combiner's design spectral range. The feed positions for the receive array in this design configuration are indicated by circular symbols in the figure. Addition of the radiators indicated by crosses can be used to improve the throughput in future implementations.

as a transition between microstrip lines and parallel-plate TEM waveguide regions. The latter is commonly referred to as the parallel-plate guide, and the microstrip planar waveguide model [5] can be used to compute its propagation and impedance properties. The transformer ratio, effective dielectric constant, and desired return loss set the necessary length of the impedance taper and were synthesized from readily available analytical forms and the response numerically simulated. A diagram of the feed aperture and spacing geometry is provided in the insert of Fig. 4 (left). In illuminating the multimode dielectric-filled parallel-plate waveguide region, the microstrip outputs play the role of the antenna apertures and need to be sized to minimize diffraction at the upper band edge.

When used as a two-dimensional antenna element, the aperture geometry not only sets the radiation pattern but also plays a role in determining the return loss [23]. This can be seen by the following consideration: The angular acceptance of the structure is constant over the band since the wavelength in the medium is less than the effective aperture width, w. Considering the scaling of the reflection amplitude as a function of feed size [24], the desire for a low return loss at the low end of the band is in tension with the needs to limit diffraction ($w < \lambda_o/\sqrt{\varepsilon_r\mu_r}$) and efficiently radiate ($w > \lambda_o/2\sqrt{\varepsilon_r\mu_r}$). This behavior effectively determines the smallest aperture size that can effectively radiate [25]. The reflection from the end of the microstrip taper scales as a power of the wavelength over the microstrip width in two dimensions and is larger than that arising from the impedance taper, which can readily be made subdominant by increasing the transformer's length. Thus, to address the reflection from the aperture, the output geometry of the aperture was apodized by adding a constant radius flare [26]. The resulting radiator element return loss, >20 dB, is achieved over a 2:1 bandwidth. Over the wavelength range where $2p < \lambda$, only the first-order diffraction occurs [27]. The influence of higher-order diffraction is mitigated through the feed apodization, the coupling geometry of arrays, and the use of absorbing boundaries on the multimode region walls.

4. Antenna Array Response

An efficient and accurate expression is desired for the evaluation of the structure's response during numerical optimization. To evaluate the antenna array's response, a classical phased array analysis approach is used. The emitters and receivers in the multimode region can be considered as a pair of opposing two-dimensional antenna arrays. By considering the Poynting vector as a function of spatial dimension, d, the following expression for the electric field is adopted for the computation of the array's response:

$$\mathbf{E}(\mathbf{r}, \theta) = \sum_{i=1}^{N_e} \frac{E_0(\theta)}{\left[1 + \left(\frac{\|\mathbf{r}\|}{w}\right)^2\right]^{(d-1)/4}} \cdot e^{j(\mathbf{k}\cdot\mathbf{r} - \varphi_{ij})}. \qquad (8)$$
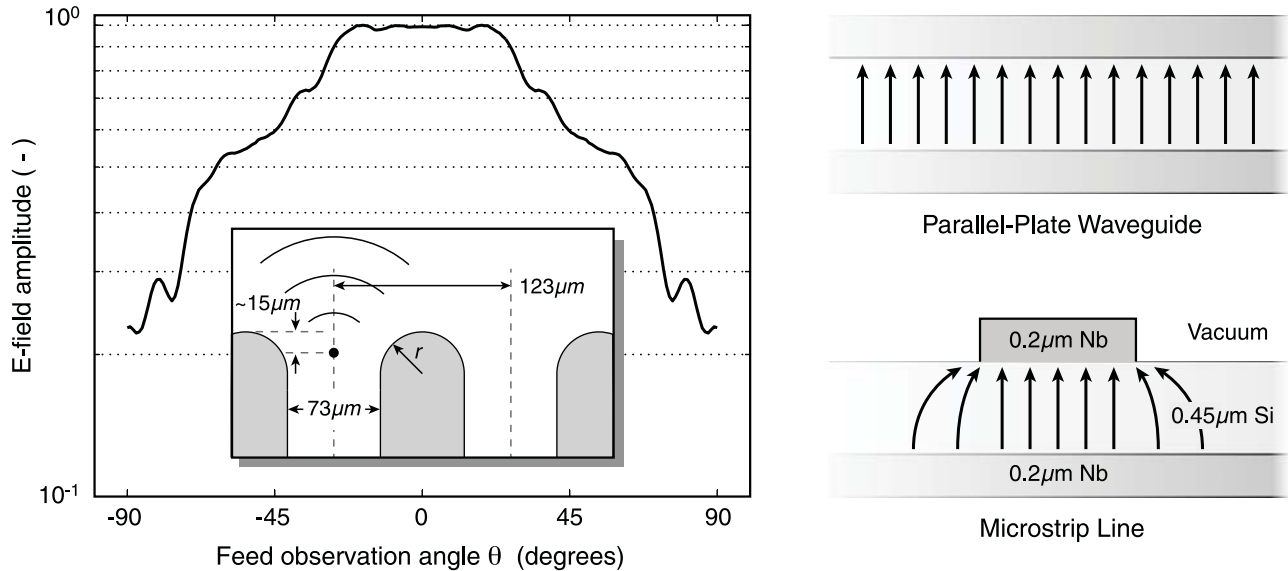
Fig. 4. (Left) The computed feed horn angular response at 430 GHz. The response of an emitting feed (aperture size 73 μm) is evaluated in the far field ($\|\mathbf{r}\| \sim 6\lambda = 438$ μm) and normalized to the magnitude of the E field at zero degrees. The feed array geometry is provided in the figure insert. The feed's phase center is indicated by a black filled circle. (Right) Cross section of the parallel-plate waveguide (upper) and microstrip (lower) transmission line geometries. The electric field is depicted with arrows to indicate the dominant modal symmetry. An adiabatic transition serves as a mode converter between these modes and defines the feed's angular response in the multimode power combined region.

Here, $\mathbf{r}$ is the separation distance vector between the center point of the i-th emitter and a point in the multimode region, E_0 is the E-field amplitude from the beam pattern angular distribution (θ) at the center of the i-th feed horn (Fig. 4), w is the effective width of the feed horns, $\mathbf{k} = (2\pi \sqrt{\varepsilon_r \mu_r}/\lambda_o) \cdot \mathbf{n}_i$ is the wavenumber vector in the medium, and $\mathbf{n}_i$ is the unity vector normal to the i-th emitter. The phase φ_{ij} includes the contributions arising from the feed aperture's phase, the phase delay, and the reference to the central emitter.

The field amplitude's dependence on radial separation is physically motivated by the behavior of the fields in transitioning from the near to the far field [28]. Close in to the feed aperture the fields are essentially constant, and in going to large distance the amplitude decreases with distance. Physically useful limiting cases to consider are $d = 3$, which yields a scaling of the E-field inversely with distance for a spherical wave, and $d = 1$, which yields a scaling independent of distance for a lossless transmission line. For $d = 2$, the case of primary interest here, it is important to note that the E-field amplitude scales as the square root of the separation distance, $\|\mathbf{r}\|$, and is anticipated for a cylindrical geometry from the asymptotic form of the Hankel functions. This expression conserves power flow, is analytic over the parameter range of interest, and is a computationally efficient representation of the structure's behavior during synthesis of the array response. The functional form and scaling indicated in Eq. (8) were validated by high-frequency structure simulation (HFSS) finite-element simulations of the structure's response with distance. These simulations were used to derive the feed aperture's effective width, w, and to determine the location of the phase center for radiation emitted by the structure.

The power is then computed from

$$P(\mathbf{r}, \theta) = \frac{1}{2\eta} \mathbf{E}^*(\mathbf{r}, \theta) \cdot \mathbf{E}(\mathbf{r}, \theta), \qquad \eta = \left(\frac{\mu_r}{\varepsilon_r}\right)^{1/2} \eta_o, \quad (9)$$

where $\eta_o = 377\Omega$ is the wave impedance of free space. Figure 5 illustrates the power distribution at 450 GHz, as was calculated from Eqs. (9) and (8). On the left side, it can be seen that the power peaks at the first stigmatic point as required, and then it quickly drops to zero along the rest of the focal plane. At separations from the feed elements greater than ~2 mm, the field transitions to the far field and the electric field amplitude is observed to asymptotically fall as $\|\mathbf{r}\|^{-1/2}$. Simulations show the power is conserved throughout the multimode region. In design example A, the ratio of the power emitted by the feed horns to the power received by the antennas is equal to ~30%. The feed response that is not intercepted by the antenna arrays is terminated by the absorber structures on the sides of the multimode region. This also enables any residual reflected power to be terminated in a controlled manner. In addition, a second-order diffraction peak, visible in the lower lefthand quadrant near the emitters, is responsible for part of this loss.

Improved performance can be achieved with different trade-offs between the antennas and the array geometry, which increase the throughput and reduce the effects of diffraction (see Table 1, design B). If the two stigmatic points are moved away from the blaze
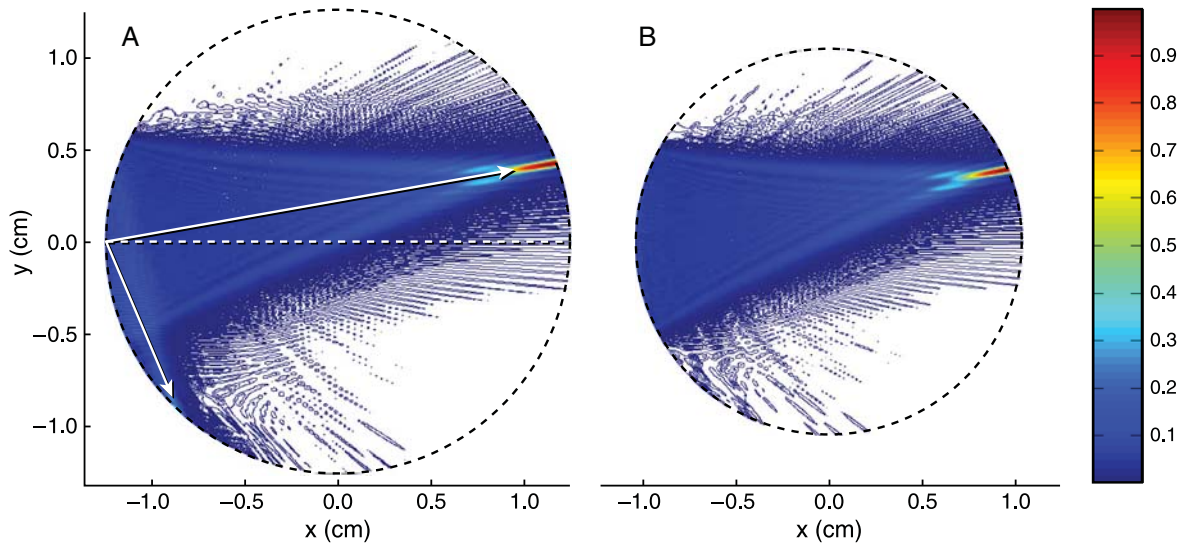
Fig. 5. Power distribution in the multimode region at a frequency of 450 GHz. On the left (Design A), the first-order peak is visible at an angle $\theta \approx 10°$, whereas the second-order diffraction peak shows up at $\theta \approx -66°$ (θ is defined in Fig. 2). In the optimized version (design B) on the right, the higher-order diffraction peak has now disappeared and the throughput is as high as 87%.

point on the optical axis along the Rowland circle by 4.2%, the instrument reaches its highest efficiency of 87% when the following applies: The radius is decreased by 16% ($R = 1.05$ cm), the number of receivers is increased by 18 ($N_r = 65$), and the emitter pitch, p, is set to 161 µm. The resulting increase in the receiver array acceptance angle is better matched to capture the transmitted beams given the apodization function of the radiators. This is the primary reason for the multimode coupling-efficiency increase observed in this example. As an aside, this change in array geometry reduces the magnitude of the second-order diffraction peak and moves it out of the range of angles of interest. For additional detail, see Fig. 5, rightmost inset.

Figure 6(a) shows the emitter antenna array's normalized power response evaluated at the three stigmatic wavelengths for the optimized multimode
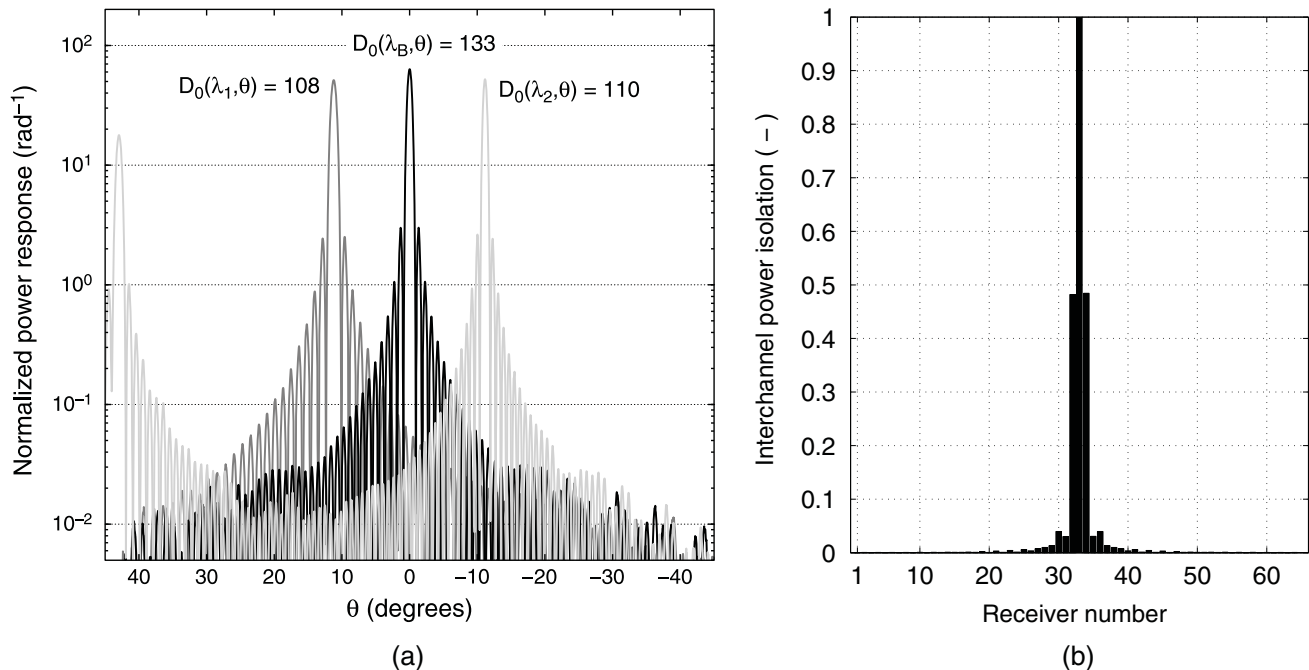

(a)

(b)

Fig. 6. Design B angular response. (a) The emitter antenna array's angular power response is normalized by the total radiated power and plotted for the three stigmatic wavelengths. The peak directivity $D_0(\lambda, \theta)$ is the angular response of the array relative to an isotropic radiator and is indicated on the plot. (b) Power isolation between the receiver channels computed for $\lambda_o \sim 560$ µm, where the power in each channel is normalized to the power in the central channel.

Table 2. Computed Coupling Efficiency ($2p > \lambda$)

Signal Frequency [GHz]	Guide Wavelength [µm]	Coupling Efficiency	
		Design A [–]	Design B [–]
450	$\lambda_1 = 195$	0.30	0.91
541	$\lambda_B = 164$	0.30	0.87
650	$\lambda_2 = 135$	0.34	0.55

region design. Table 2 summarizes the coupling efficiency between receiver and transmitter antenna arrays for the two design variations considered in this section. The interchannel power isolation is presented in Fig. 6(b) for the center channel of the optimized design. The observed finite isolation, <0.48, arises from the design goal to fully sample the spectrum and maximize the structure's optical throughput. The resulting signal correlation can be addressed in calibration of the spectrometer response. Finally, the RMS phase error now reaches a maximum of 0.011 at $\beta = 75.8°$ and 104.3° and vanishes at the three stigmatic points ($\beta = 67.8°$, 90° and 112.2°).

5. Conclusions

A theory and design methodology has been described for µ-Spec, a superconducting microstrip-based direct-detection spectrometer, in which the phase retardation is generated by propagation through transmission lines of different length. A proof-of-concept design was realized to demonstrate the feasibility of the instrument. The location of the three stigmatic points was chosen to minimize the overall RMS phase error for all spectrometer outputs, whereas the location of both radiators and receivers was found by setting the light path function equal to integer multiples of the three wavelengths associated with the three stigmatic points. The structure's response was evaluated through an E-field model validated by finite-element simulations. The results show that, through a geometric optimization of the instrument, a maximum throughput of ~90% can be achieved in the multimode region. The attributes of this design approach, namely reduced spectrometer envelope and high throughput, have the potential to enable a new class of space-born instrumentation that will reveal new details of the early universe.

References

1. M. W. Werner, T. L. Roellig, F. J. Low, G. H. Rieke, M. Rieke, W. F. Hoffmann, E. Young, J. R. Houck, B. Brandl, G. G. Fazio, J. L. Hora, R. D. Gehrz, G. Helou, B. T. Soifer, J. Stauffer, J. Keene, P. Eisenhardt, D. Gallagher, T. N. Gautier, W. Irace, C. R. Lawrence, L. Simmons, J. E. Van Cleve, M. Jura, E. L. Wright, and D. P. Cruikshank, "The Spitzer space telescope mission," Astrophys. J., Suppl. Ser. **154**, 1–9 (2004).
2. G. L. Pilbratt, J. R. Riedinger, T. Passvogel, G. Crone, D. Doyle, U. Gageur, A. M. Heras, C. Jewell, L. Metcalfe, S. Ott, and M. Schmidt, "Herschel Space Observatory, an ESA facility for far-infrared and submillimeter astronomy," Astron. Astrophys. **518**, 1–6 (2010).
3. M. F. Kessler, J. A. Steinz, M. E. Anderegg, J. Clavel, G. Drechsel, P. Estaria, J. Faelker, J. R. Riedinger, A. Robson, B. G. Taylor, and S. Ximénez de Ferrán, "The Infrared Space Observatory (ISO)," Astron. Astrophys. **315**, L27–L31 (1996).
4. T. Nakagawa, H. Matsuhara, and Y. Kawakatsu, "The next-generation infrared space telescope SPICA," Proc. SPIE **8442**, 844200 (2012).
5. D. M. Pozar, *Microwave Engineering*, 3rd ed. (Wiley, 2005), pp. 98–106, 143–149.
6. H. A. Rowland, "On concave gratings for optical purposes," Philos. Mag. **16**(99), 197–210 (1883).
7. H. W. Yen, H. R. Friedrich, R. J. Morrison, and G. L. Tangonan, "Planar Rowland spectrometer for fiber-optic wavelength demultiplexing," Opt. Lett. **6**, 639–641 (1981).
8. R. März and C. Cremer, "On the theory of planar spectrographs," J. Lightwave Technol. **10**, 2017–2022 (1992).
9. M. Wu and Y. J. Chen, "Design considerations for Rowland circle gratings used in photonic integrated devices for WDM applications," J. Lightwave Technol. **12**, 1939–1942 (1994).
10. P. Muñoz, D. Pastor, J. Capmany, and A. Martínez, "Geometrical optimization of the transmission and dispersion properties of arrayed waveguide gratings using two stigmatic point mountings," Opt. Express **11**, 2425–2432 (2003).
11. B. J. Naylor, "Broadband millimeter-wave spectroscopy with Z-Spec: an unbiased molecular-line survey of the starburst galaxy M82," Ph.D. Thesis (California Institute of Technology, 2008).
12. C. M. Bradford, B. J. Naylor, J. Zmuidzinas, J. J. Bock, J. Gromke, H. Nguyen, M. Dragovan, M. Yun, L. Earle, J. Glenn, H. Matsuhara, P. A. R. Ade, and L. Duband, "WaFIRS, a waveguide far-IR spectrometer: enabling spectroscopy of high-z galaxies in the far-IR and submillimeter," Proc. SPIE **4850**, 1137–1147 (2003).
13. C. M. Bradford, P. Ade, J. Aguirre, J. J. Bock, L. Duband, L. Earle, J. Glenn, H. Matsuhara, B. J. Naylor, H. Nguyen, M. Yun, and J. Zmuidzinas, "Z-Spec: a broadband millimeter-wave grating spectrometer—design, construction, and first cryogenic measurements," Proc. SPIE **5408**, 257–267 (2004).
14. L. Earle, P. Ade, J. Aguirre, R. Aikin, J. Battle, J. Bock, C. M. Bradford, M. Dragovan, L. Duband, J. Glenn, G. Griffin, V. Hristov, P. Maloney, H. Matsuhara, B. Naylor, H. Nguyen, M. Yun, and J. Zmuidzinas, "Z-Spec: a broadband, direct-detection, millimeter-wave spectrometer—instrument status and first results," Proc. SPIE **6275**, 1–9 (2006).
15. W. Rotman and R. F. Turner, "Wide-angle microwave lens for line source applications," IEEE Trans. Antennas Propag. **11**, 623–632 (1963).
16. T. Katagi, S. Mano, and S. I. Sato, "An improved design method of Rotman lens antennas," IEEE Trans. Antennas Propag. **32**, 524–527 (1984).
17. R. C. Hansen, "Design trades for Rotman lenses," IEEE Trans. Antennas Propag. **39**, 464–472 (1991).
18. C. M. Rappaport and A. I. Zaghloul, "Multifocal bootlace lens design concepts: a review," in *Proceedings of IEEE Antennas and Propagation Society International Symposium*, **2B** (IEEE, 2005), pp. 39–42.
19. F. W. Gembicki, "Vector optimization for control with performance and parameter sensitivity indices," Ph.D. Thesis (Case Western Reserve University, 1974).
20. A. R. Kerr, "Surface impedance of superconductors and normal conductors in EM simulators," National Radio Astronomy Observatory, Millimeter Array (MMA) Technical Report, Memo No. 245, January 7, 1999.
21. R. E. Collin, *Foundations for Microwave Engineering* (McGraw-Hill, 1992), Section 5.19, pp. 383–386.
22. R. P. Hecken, "A near-optimum matching section without discontinuities," IEEE Trans. Microwave Theory Tech. **20**, 734–739 (1972).

23. G. Matthaei, L. Young, and E. M. T. Jones, *Microwave Filters, Impedance-Matching Networks and Coupling Structures* (McGraw-Hill, 1964), pp. 290–291.
24. S. Silver, *Microwave Antenna Theory and Design* (McGraw-Hill, 1949), pp. 439–448, 453–457.
25. S. H. Moseley, E. J. Wollack, and G. Hinshaw, "Limits to the efficiency of imaging systems," in *Proceedings of the Far-Infrared, sub-mm, and mm Detector Technology Workshop*, J. Wolf, J. Farhoomand, and C. R. McCreight, eds. (NASA/CP-211408, 2002), pp. 388–391.
26. J. C. Mather, "Broad-band flared horn with low sidelobes," IEEE Trans. Antennas Propag. **29**, 967–969 (1981).
27. R. C. Hansen, *Phased Array Antennas* (Wiley, 1998), p. 15.
28. J. C. Slater and N. H. Frank, *Introduction to Theoretical Physics* (McGraw-Hill, 1933), p. 317.